



Article

Synthesis of Highly Monodisperse Nickel and Nickel Phosphide Nanoparticles

Hyungjin Cho ¹, Nohyun Lee ² and Byung Hyo Kim ^{1,3,*} ¹ Department of Organic Materials and Fiber Engineering, Soongsil University, Seoul 06978, Korea² School of Advanced Materials Engineering, Kookmin University, Seoul 02707, Korea³ Department of Green Chemistry and Materials Engineering, Soongsil University, Seoul 06978, Korea

* Correspondence: byunghyokim@ssu.ac.kr; Tel.: +82-2-829-8218

Abstract: Nickel and nickel phosphide nanoparticles are highly useful in various fields, owing to their catalytic and magnetic properties. Although several synthetic protocols to produce nickel and nickel phosphide nanoparticles have been previously proposed, controllable synthesis of nanoparticles using these methods is challenging. Herein, we synthesized highly monodisperse nickel and nickel phosphide nanoparticles via thermal decomposition of nickel–oleylamine–phosphine complexes in organic solvents. The size and composition of the nickel and nickel phosphide nanoparticles were easily controlled by changing the aging temperature, precursor concentration, and phosphine surfactant type. Large-sized monodisperse nickel nanoparticles obtained using our method were successfully applied for the purification of histidine-tagged proteins.

Keywords: nanoparticles; nickel; nickel phosphide; his-tagged protein



Citation: Cho, H.; Lee, N.; Kim, B.H. Synthesis of Highly Monodisperse Nickel and Nickel Phosphide Nanoparticles. *Nanomaterials* **2022**, *12*, 3198. <https://doi.org/10.3390/nano12183198>

Academic Editor: Enrico Ferrari

Received: 16 August 2022

Accepted: 9 September 2022

Published: 14 September 2022

Publisher's Note: MDPI stays neutral with regard to jurisdictional claims in published maps and institutional affiliations.



Copyright: © 2022 by the authors. Licensee MDPI, Basel, Switzerland. This article is an open access article distributed under the terms and conditions of the Creative Commons Attribution (CC BY) license (<https://creativecommons.org/licenses/by/4.0/>).

1. Introduction

The synthesis of magnetic nanoparticles is important because of their broad applications in magnetic resonance imaging, drug delivery, magnetic separation, catalysis, and magnetic storage devices [1–5]. As physical properties of nanoparticles are affected by their size and shape, synthetic methods allowing the control of particle size, size distribution, and particle shape are strongly desired [6–8]. Nickel and nickel oxide nanoparticles are widely used as catalysts [9,10], in magnetic separation of histidine-tagged proteins [11], in resistive random access memory [12], and as superconductors [13]. Nickel nanoparticles have been previously synthesized using sonochemistry [14], reduction [15–17], decomposition of organometallic compounds or metal salts [18,19], and electrochemical methods [20]. However, nanoparticles synthesized using these methods are polydisperse, have low crystallinity, and are prone to aggregation. Monodisperse nickel nanoparticles have also been synthesized using the thermal decomposition of organometallic complexes in organic solvents. However, the diameter of the monodisperse nickel nanoparticles synthesized via the abovementioned procedures is usually smaller than 10 nm [21–24], and small nanoparticles are fully oxidized to antiferromagnetic nickel oxide nanoparticles with a low magnetic moment [24]. Nickel phosphide nanoparticles are also important materials for catalysis, supercapacitors, and electrocatalysis [25–28].

Metal phosphide nanoparticles have been previously synthesized using phosphine [29–33], phosphate salts [34], and pure phosphorous as phosphorous sources [35,36]. In recent works, nickel nanoparticles have often been used as scaffolds for producing nickel phosphide nanoparticles [37,38]. The reported procedures, however, are tedious, and the resulting nanoparticles are polydisperse.

A simple method for the synthesis of monodisperse nickel and nickel phosphide nanoparticles is presented in this report. The resulting nickel nanoparticles are highly monodisperse and sufficiently large to maintain a pure nickel core even after oxidation

in air. Moreover, both nickel and nickel phosphide nanoparticles can be obtained using a single synthetic scheme reported here, only at different aging temperatures.

2. Materials and Methods

2.1. Materials

Nickel(II) acetylacetonate ($\text{Ni}(\text{acac})_2$, 90%), octyl ether (99%), trioctyl phosphine (TOP, 90%), 1-octadecene (90%), and oleic acid (90%) were purchased from Sigma-Aldrich (St. Louis, MO, USA). Tributyl phosphine (TBP) was purchased from Fluka (Charlotte, NC, USA). Oleyl amine was purchased from Acros. All chemicals were used without further purification.

Histidine-tagged green fluorescent protein (GFP) and PE-Cy5-conjugated normal mouse IgG1 were purchased from Santa Cruz Biotechnology (Dallas, TX, USA) and Upstate, respectively.

2.2. Methods

2.2.1. Synthesis of 9 nm Nickel Nanoparticles

Ni-oleylamine complex was prepared by reacting 1.55 g of oleylamine with 0.257 g of $\text{Ni}(\text{acac})_2$ at 100 °C for 30 min under an inert atmosphere. Dioctyl ether (6 mL) was injected into the Ni-oleylamine complex, and the solution was degassed for 1 h at 100 °C under vacuum. TBP (0.3 mL) was injected into the nickel complex solution under an argon atmosphere. The solution was heated to 250 °C with a heating rate of 2 °C/min and aged at the same temperature for 30 min. At approximately 200 °C, the color of the solution started to change from bluish-green to black, indicating the formation of nickel nanoparticles. After aging, the product was rapidly cooled to 70 °C. Oleic acid (2 mL) was added to the product under argon flow to stabilize the nanoparticle dispersion. Nanoparticles were precipitated by adding a 1:2 mixture of excess ethanol and acetone. The nanoparticles were dispersed in hydrophobic solvents, such as hexane or chloroform.

2.2.2. Synthesis of 13 nm Nickel Nanoparticles

Dioctyl ether (5 mL) was injected into the Ni-oleylamine complex, and the solution was degassed for 1 h at 100 °C under vacuum. TBP (0.3 mL) was injected into the nickel complex solution under an argon atmosphere. The solution was then heated to 250 °C with a heating rate of 2 °C/min and aged at the same temperature for 30 min.

2.2.3. Synthesis of Ni_{12}P_5 Nanoparticles

Dioctyl ether (5 mL) was injected into the Ni-oleylamine complex, and the solution was degassed for 1 h at 100 °C under vacuum. TBP (0.3 mL) was injected into the nickel complex solution under an argon atmosphere. The solution was then heated to 280 °C with a heating rate of 2 °C/min and aged at the same temperature for 30 min.

2.2.4. Ligand Exchange of Nickel/Nickel Oxide (Ni/NiO) Nanoparticles

The nanoparticles (200 mg) oxidized in air were dispersed in an imidazole solution in chloroform (0.1 g/mL, 5 mL) and stirred for 6 h. The ligand-exchanged nanoparticles were collected by centrifugation after adding n-hexane.

2.2.5. Reaction of Ni/NiO Nanoparticles with Proteins

The imidazol-stabilized oxidized Ni nanoparticles (60 µg) were mixed with 250 µL of protein solution with a concentration of 30 µg/mL. The protein solutions were prepared by dissolving histidine-tagged GFP or PE-Cy5-conjugated normal mouse IgG1 antibodies in PBS. The mixture containing Ni/NiO nanoparticles and fluorescent proteins was incubated by shaking for 30 min. The Ni/NiO nanoparticles and bound proteins were purified using a magnet. The purified particles and proteins were redispersed in 250 µL of imidazole solution (0.1 g/mL). The proteins bound to the Ni/NiO nanoparticles were released by shaking for 30 min.

2.2.6. Characterization of Materials

Transmission electron microscopy (TEM) and high-resolution TEM (HRTEM) images were obtained by JEOL EM-2010 and JEOL EM-2100F at an accelerating voltage of 200 kV. X-ray diffraction (XRD) patterns were acquired using a Rigaku Dmax 2500 diffractometer using monochromatized Cu-K α radiation at 40 kV and 200 mA. The hydrodynamic size of the ligand-exchanged nanoparticles was characterized by Otsuka DLS-8000. The magnetization measurements were performed using an MPMS 5XL Quantum Design superconducting quantum interference device (SQUID) magnetometer. Photoluminescence spectra were collected on a Perkin-Elmer LS 50 B spectrometer at excitation wavelengths of 400 nm (for GFP) and 630 nm (for Cy5).

3. Results and Discussion

Analysis of Ni Nanoparticles

TEM images of Ni nanoparticles synthesized using TBP as a surfactant are shown in Figure 1. The images show highly monodisperse Ni nanoparticles obtained without any size selection. The large-area two-dimensional assembly of nanoparticles confirmed their monodispersity, as shown in Figure S1. The particle sizes were controlled by regulating the precursor concentration: nanoparticles with diameters of 9 and 13 nm (Figure 1a,b) were synthesized at precursor concentrations of 167 and 200 mM, respectively. Size distribution histograms proved that the particles were very monodisperse, with the coefficient of variation for size not exceeding 4% (Figure 1c,d).

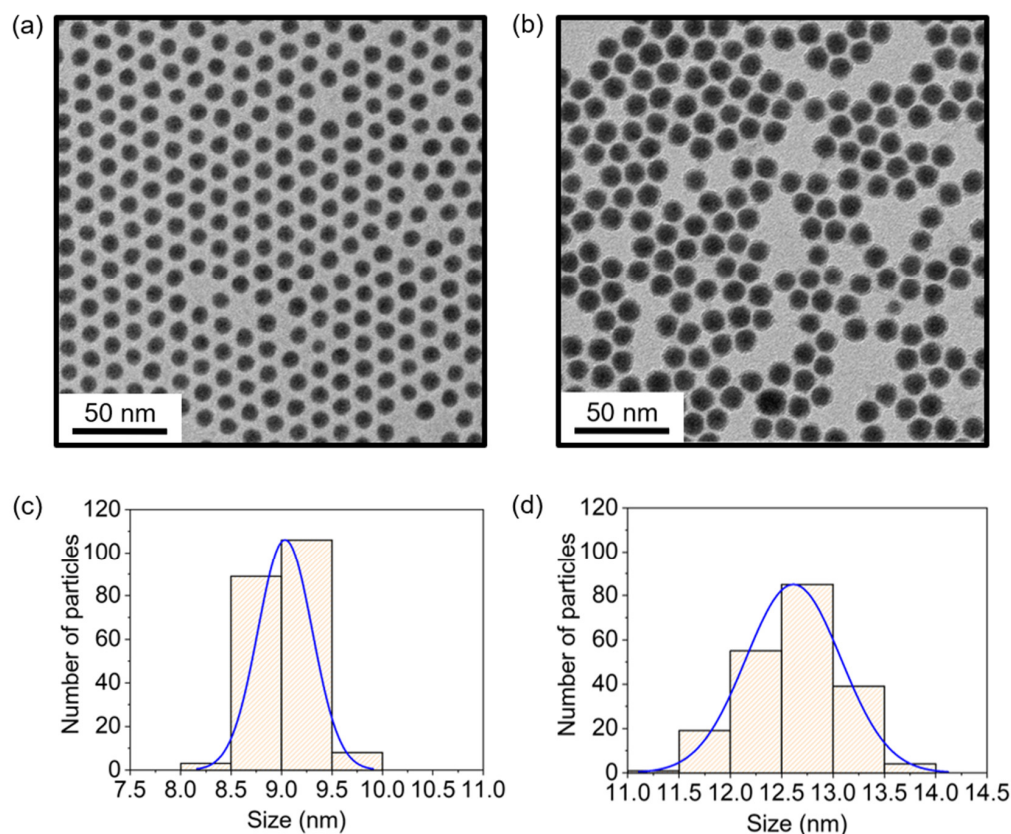


Figure 1. TEM images of (a) 9 nm and (b) 13 nm nickel nanoparticles obtained at precursor concentrations of 167 and 200 mM, respectively. Scale bars are 50 nm. The corresponding size histograms are displayed in (c,d). The average diameters of the nanoparticles were (c) 9.03 nm and (d) 12.61 nm. The standard deviations were (c) 2.97% (0.268 nm) and (d) 3.67% (0.463 nm). Blue lines are Gaussian fitted lines. To ensure the accuracy of size measurement, we measured the sizes of 208 individual particles for each batch.

The HRTEM image of the 13 nm nanoparticles observed one month after the synthesis revealed the polycrystalline structure of the nickel core and nickel oxide shell (Figure S2). With continuous exposure to air, nickel atoms on the surface of the nanoparticles are oxidized and form a ~3 nm thick nickel oxide layer, owing to the limited diffusion depth of oxygen [39]. While large nickel particles are partially oxidized, nanoparticles smaller than 7 nm are completely oxidized to nickel oxide nanoparticles [40,41]. The HRTEM image showed voids at the interface between the nickel and nickel oxide layers and bridges in the voids. The voids and bridges between the two components are typical features of the nanoscale Kirkendall effect. The Kirkendall effect is an atomic transfer phenomenon at the interface of a diffusion couple [9,42]. When atomic diffusion occurs through vacancy exchange, the outward flow of fast-moving cations and inward flow of slow-moving oxide anions produce a metal/metal oxide core/shell structure with voids at the interface between the metal and metal oxide. The Kirkendall effect can occur at room temperature if atomic diffusivity is low for a sufficiently long time. Upon exposure to air for a month, the 13 nm nickel nanoparticles changed to 16 nm Ni/NiO nanoparticles, as shown in the HRTEM image (Figure S2). This peculiar change may also be the result of the Kirkendall effect. The core nickel cations moved faster than the outer oxide anions. As a result, a nickel oxide layer was formed, and the size of the nanoparticles increased.

The crystal structures of the nickel nanoparticles were characterized using XRD. The large and broad (111) peak at 44° and the small (220) peak at 77° in the XRD pattern in Figure 2c indicate that the particles consisted of face-centered-cubic (fcc) Ni. The broad peaks imply that the particles had a small grain size. The grain size calculated using the Scherrer equation was 2.2 nm [43], which was much smaller than the core size measured by TEM (~9 nm), indicating that the core material had a polycrystalline morphology. The polycrystalline nature of the obtained nickel nanoparticles was also identified using HRTEM (Figure S2). Nickel oxide peaks were absent in the XRD pattern because the metal oxide shell formed through the Kirkendall effect has amorphous morphology [44]. The oxidation of nickel was confirmed using X-ray photoelectron spectroscopy (XPS). The XPS data exhibited two peaks related to Ni²⁺ ions on the surface (Figure S3).

Phosphine surfactants, TBP and TOP, were used to synthesize nickel nanoparticles. The use of TOP as a surfactant in a 200 mM precursor produced nickel nanoparticles with a size of 10 nm. At the same time, 13 nm nickel nanoparticles were synthesized using TBP as a surfactant (Figure S4). During aging, bulky TOP molecules limit the growth of nanoparticles, resulting in the formation of small particles [22].

The chemical composition of nanoparticles was controlled by varying the aging temperature. The XRD patterns of the nanoparticles aged at 240 and 280 °C are shown in Figure 2c,d. The XRD patterns demonstrated that the nanoparticles aged at 280 °C consisted of Ni₁₂P₅ with (440), (312), (510), and (004) peaks and that those aged at 240 °C were fcc Ni particles. Ni₁₂P₅ particles had hollow structures (Figures 2b and S5); the phosphorus source for their formation was trialkyl phosphine. Phosphine has been previously used either as a phosphorus source for the synthesis of metal phosphide nanoparticles [33] or as a surfactant for metal nanoparticles [45,46]. In most cases, when trialkyl phosphine was used as a phosphorus source, nanoparticles are synthesized at temperatures higher than 280 °C. Above 280 °C, the carbon–phosphorus bonds in trialkyl phosphines are dissociated owing to the high thermal energy. Free phosphorus atoms participate in the formation of nanoparticles, resulting in the formation of metal phosphides. Moreover, the surface metal atoms of the nanoparticles can act as catalysts to break carbon–phosphorus bonds and promote phosphide formation reactions [32]. At aging temperatures below 250 °C, trialkyl phosphines act as surfactants [22,45]. Below 250 °C, carbon–phosphorus bonds in trialkyl phosphines remain intact because of low thermal energy. Therefore, at low temperatures, nickel nanoparticles were obtained, whereas at high temperatures, nickel phosphide nanoparticles were synthesized, as shown in the XRD patterns. The differential scanning calorimetry (DSC) data for TBP support this explanation (Figure S6). Two

endothermic peaks that indicate the dissociation of the carbon–phosphorus bond were observed at 255 and 296 °C in the DSC results.

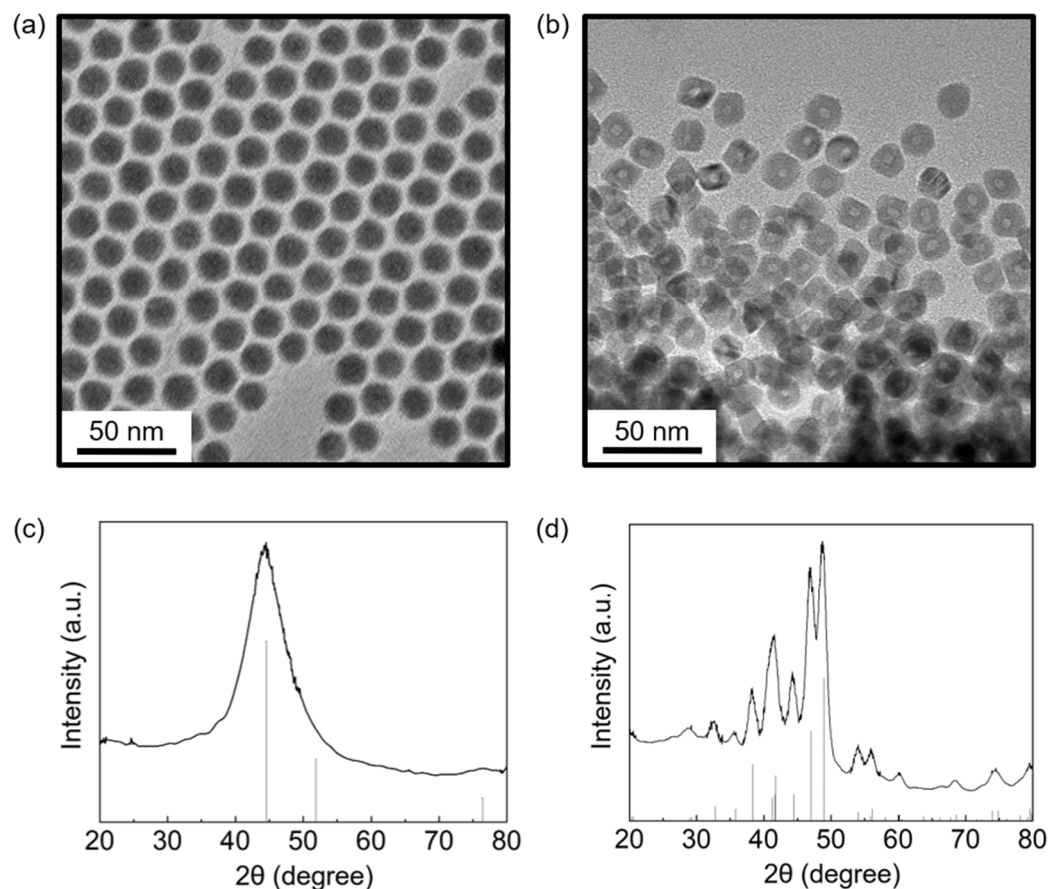


Figure 2. TEM images of (a) Ni and (b) Ni_{12}P_5 synthesized at (a) 240 and (b) 280 °C (precursor concentration = 200 mM, surfactant: TBP, solvent: dioctyl ether) and XRD spectra of (c) Ni (a, JCPDS number 87-0712) and (d) Ni_{12}P_5 (b, JCPDS number 74-1381) nanoparticles.

The magnetic properties of nickel nanoparticles are dependent on their size. The magnetization–magnetic field curve of 13 nm Ni nanoparticles measured using SQUID showed that the saturation magnetization of the nanoparticles at 8000 Oe was 2.8 emu/g (Figure 3), which is much smaller than the saturation magnetization of bulk nickel (56 emu/g). The small magnetization of nickel nanoparticles is also reported in the literature on the synthesis of nickel nanoparticles [14,47–49]. This result can be explained by several reasons. First, a small volume of the magnetic region may cause small magnetization. Ni nanoparticles changed into a Ni/NiO core/shell structure via surface oxidation (Figure S2). Ni/NiO nanoparticles mostly consist of an antiferromagnetic nickel oxide layer, which has much weaker magnetic properties than Ni. Second, the polycrystalline morphology may reduce magnetization [14,49]. Incomplete coordination of nickel atoms on the surface or grain boundaries of particles leads to spin disordering. This disorder has been interpreted as the cause of the small saturation magnetization. Third, phosphorus impurities may be responsible for reduced magnetism. As discussed in the previous section, nickel phosphide nanoparticles were synthesized through the breakage of the carbon–phosphorus bonds in trialkyl phosphine at temperatures higher than 280 °C. At the same time, bond breakage can still occur below 280 °C because of the distribution of thermal energy. Therefore, we assumed that the phosphorus atoms derived from phosphine acted as impurities. The exchange coupling can be interrupted by impurities, resulting in decreased magnetization [50].

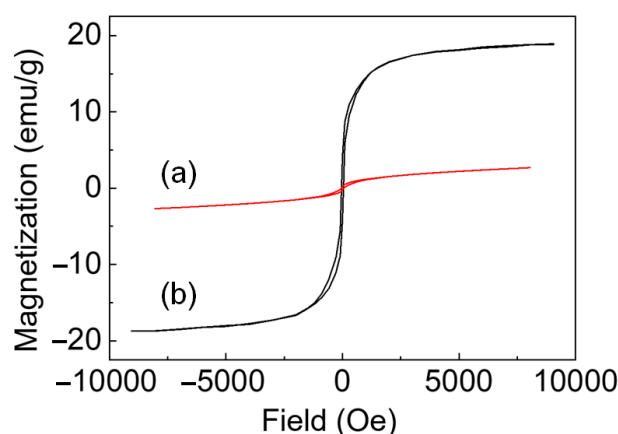


Figure 3. Magnetization (M)–magnetic field (H) curve for Ni nanoparticles measured by SQUID at 5 K for (a) 13 nm and (b) 18 nm Ni nanoparticles.

To obtain nanoparticles with high magnetism, both the crystallinity and size of the particles should be increased while reducing the amount of impurities. When a smaller amount of phosphine was used, larger particles with high crystallinity and fewer impurities were obtained. Because phosphine molecules can induce the decomposition of the Ni–oleylamine complex [21], the use of a small amount of phosphine leads to the slow nucleation of nickel. The smaller number of nuclei formed during slow nucleation grew to larger particles because of the higher number of atoms per nuclei [51]. At the same time, phosphorus impurities expand the lattice parameter. When more phosphine was used, the position of the Ni(111) peak in the XRD patterns shifted to a lower angle, and the calculated lattice parameter increased. The relationship between the amount of phosphine and the lattice parameter is shown in Figure S7 and Table S1. The particles synthesized with the lowest amount of impurities (precursor: phosphine = 1:0.6) were the largest (18 nm). The 18 nm nickel nanoparticles were highly attracted to magnets and showed a saturation magnetization of 19 emu/g and a blocking temperature of 167 K (Figures 3, S8 and S9). Previous literature reported that carbon impurity can be inserted into Ni at the aging temperature we used [52].

Nickel nanoparticles were applied for the magnetic separation of histidine-tagged proteins, which requires Ni^{2+} cations. Ni^{2+} ions have a high affinity for polyhistidine and are exposed at the surface of the nickel nanoparticles after the oxidation of nickel to nickel oxide under air exposure [11]. For the biomedical protein separation, we transformed the hydrophobic nickel nanoparticles into hydrophilic particles to ensure their dispersion in the water phase using ligand exchange (Figure S10). For the purpose of protein separation by the Ni/NiO nanoparticles, we used polyhistidine-tagged GFP because the fluorescent property of the protein enables visualization and characterization of the successful separation of the protein. In a typical experiment, nickel nanoparticles were incubated with histidine-tagged GFP for 30 min and then separated from the supernatant through the application of the magnetic field. The fluorescence emission of the supernatant was significantly lower (~5%) than that of the initial solution (Figure 4). The histidine-tagged GFP-bound nanoparticles were then incubated with imidazole solution to release GFP proteins from the nanoparticles. The fluorescence emission recovered to 71% of the initial solution after the release of bound GFP proteins. This result indicated the efficient binding and separation of histidine-tagged GFP by Ni/NiO nanoparticles. Although the nanoparticles are capped with ligands, the purification of histidine-tagged proteins is activated by the partially exposed Ni^{2+} ions on the surfaces. It has been known that the nanoparticle surface is not fully coordinated with ligands due to the geometric factor, especially for bulky ligands such as imidazole. In addition, adsorption and desorption of ligands on the nanoparticle surface are reversible reactions; thus, Ni^{2+} ions can be exposed during adsorption and desorption. As a control experiment, we conducted an identical experiment using normal mouse IgG1

labeled with red-emitting Cy5 without a polyhistidine residue instead of histidine-tagged GFP. For the conventional dye-labeled protein, we observed only a 12% decrease in the fluorescence intensity, indicating a small extent of nonspecific protein binding.

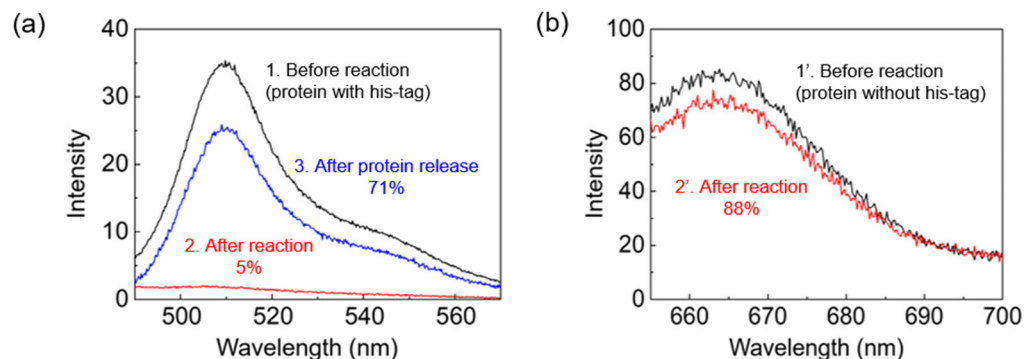


Figure 4. (a) Fluorescence spectra for the solutions of histidine-tagged GFP (1) before and (2) after the treatment with Ni/NiO nanoparticles and (3) after the treatment of protein-bound Ni/NiO nanoparticles with imidazole solution. (b) Fluorescence spectra for the solutions of normal mouse IgG1 labeled with Cy5 (1') before and (2') after the treatment with Ni/NiO nanoparticles.

4. Conclusions

We synthesized highly monodisperse nickel nanoparticles, which were transformed into a Ni/NiO core/shell structure via oxidation of the surface nickel atoms. We also synthesized nickel phosphide nanoparticles using the same procedure but at a higher aging temperature. At a higher temperature, the carbon–phosphorus bonds in alkyl phosphines break, generating free phosphorus atoms to participate in the formation of nickel phosphide nanoparticles. The resulting nickel nanoparticles can be used for the magnetic separation of histidine-tagged proteins.

Our synthetic system is simple and highly reproducible. As our synthesis does not require a hot injection step, it can be used to synthesize nickel particles on a large scale. We were able to obtain 1.4 g of nickel nanoparticles in a single batch using 10 times more reagent than reported here.

Supplementary Materials: The following supporting information can be downloaded at: <https://www.mdpi.com/article/10.3390/nano12183198/s1>, Figure S1: Large-area TEM image of 9 nm nickel nanoparticles.; Figure S2: TEM image of polycrystalline Ni/NiO core/shell nanoparticles after oxidation of nickel nanoparticles.; Figure S3. X-ray photoelectron spectroscopy (XPS) spectrum of 9 nm nickel nanoparticles.; Figure S4. TEM images of (a) 10 nm and (b) 13 nm Ni nanoparticles, synthesized using TOP and TBP as surfactants, respectively.; Figure S5. HRTEM images of hollow Ni₁₂P₅ nanoparticles synthesized at 280 °C.; Figure S6. DSC data of TBP.; Figure S7. XRD patterns of (a) 13 nm, (b) 15 nm, (c) 17 nm, and (d) 18 nm Ni nanoparticles synthesized when the precursor to phosphine ratio was 1:1.2, 1:1.0, 1:0.8, and 1:0.60, respectively.; Table S1. Lattice parameters of Ni nanoparticles obtained by varying precursor to phosphine ratio.; Figure S8. Temperature dependence of magnetization measured with 100 Oe for (a) 13 nm and (b) 18 nm Ni nanoparticles.; Figure S9. Magnetization–magnetic field curves of Ni nanoparticles measured by SQUID at 300 K for (a) 18 nm and (b) 13 nm Ni particles.; Figure S10. The hydrodynamic size distribution of nickel nanoparticles after the ligand exchange process as measured by DLS.

Author Contributions: Conceptualization, B.H.K.; methodology, H.C., N.L. and B.H.K.; formal analysis, H.C. and B.H.K.; investigation, B.H.K.; resources, B.H.K.; data curation, H.C.; writing—original draft preparation, B.H.K.; writing—review and editing, H.C. and B.H.K.; visualization, H.C.; supervision, B.H.K.; project administration, B.H.K.; funding acquisition, B.H.K. All authors have read and agreed to the published version of the manuscript.

Funding: This research was funded by National Research Foundation of Korea (NRF), grant number NRF-2021R1C1C1014339.

Institutional Review Board Statement: Not applicable.

Informed Consent Statement: Not applicable.

Data Availability Statement: The data presented in this study are available on request from the corresponding author.

Conflicts of Interest: The authors declare no conflict of interest.

References

1. Hyeon, T. Chemical synthesis of magnetic nanoparticles. *Chem. Commun.* **2003**, *34*, 927–934. [[CrossRef](#)] [[PubMed](#)]
2. Heydari Sheikh Hossein, H.; Jabbari, I.; Zarepour, A.; Zarrabi, A.; Ashrafzadeh, M.; Taherian, A.; Makvandi, P. Functionalization of magnetic nanoparticles by folate as potential MRI contrast agent for breast cancer diagnostics. *Molecules* **2020**, *25*, 4053. [[CrossRef](#)] [[PubMed](#)]
3. Kudr, J.; Haddad, Y.; Richtera, L.; Heger, Z.; Cernak, M.; Adam, V.; Zitka, O. Magnetic nanoparticles: From design and synthesis to real world applications. *Nanomaterials* **2017**, *7*, 243. [[CrossRef](#)] [[PubMed](#)]
4. Wu, L.; Mendoza-Garcia, A.; Li, Q.; Sun, S. Organic phase syntheses of magnetic nanoparticles and their applications. *Chem. Rev.* **2016**, *116*, 10473–10512. [[CrossRef](#)] [[PubMed](#)]
5. Kim, D.; Lee, N.; Park, M.; Kim, B.H.; An, K.; Hyeon, T. Synthesis of Uniform Ferrimagnetic Magnetite Nanocubes. *J. Am. Chem. Soc.* **2009**, *131*, 454–455. [[CrossRef](#)] [[PubMed](#)]
6. Sun, S.; Zeng, H. Size-Controlled Synthesis of Magnetite Nanoparticles. *J. Am. Chem. Soc.* **2002**, *124*, 8204–8205. [[CrossRef](#)]
7. Park, J.; An, K.; Hwang, Y.; Park, J.-G.; Noh, H.-J.; Kim, J.-Y.; Park, J.-H.; Hwang, N.-M.; Hyeon, T. Ultra-large-scale syntheses of monodisperse nanocrystals. *Nat. Mater.* **2004**, *3*, 891–895. [[CrossRef](#)]
8. Issa, B.; Obaidat, I.M.; Albiss, B.A.; Haik, Y. Magnetic nanoparticles: Surface effects and properties related to biomedicine applications. *Int. J. Mol. Sci.* **2013**, *14*, 21266–21305. [[CrossRef](#)]
9. Song, X.; Gao, L. Facile Synthesis and Hierarchical Assembly of Hollow Nickel Oxide Architectures Bearing Enhanced Photocatalytic Properties. *J. Phys. Chem. C* **2008**, *112*, 15299–15305. [[CrossRef](#)]
10. Zhu, L.; Jiang, Y.; Zheng, J.; Zhang, N.; Yu, C.; Li, Y.; Pao, C.W.; Chen, J.L.; Jin, C.; Lee, J.F. Ultrafine Nanoparticle-Supported Ru Nanoclusters with Ultrahigh Catalytic Activity. *Small* **2015**, *11*, 4385–4393. [[CrossRef](#)]
11. Lee, I.S.; Lee, N.; Park, J.; Kim, B.H.; Yi, Y.-W.; Kim, T.; Kim, T.K.; Lee, I.H.; Paik, S.R.; Hyeon, T. Ni/NiO Core/Shell Nanoparticles for Selective Binding and Magnetic Separation of Histidine-Tagged Proteins. *J. Am. Chem. Soc.* **2006**, *128*, 10658–10659. [[CrossRef](#)] [[PubMed](#)]
12. Oka, K.; Yanagida, T.; Nagashima, K.; Tanaka, H.; Kawai, T. Nonvolatile Bipolar Resistive Memory Switching in Single Crystalline NiO Heterostructured Nanowires. *J. Am. Chem. Soc.* **2009**, *131*, 3434–3435. [[CrossRef](#)]
13. Lang, J.-W.; Kong, L.-B.; Wu, W.-J.; Luo, Y.-C.; Kang, L. Facile approach to prepare loose-packed NiO nano-flakes materials for supercapacitors. *Chem. Commun.* **2008**, *35*, 4213–4215. [[CrossRef](#)] [[PubMed](#)]
14. Koltypin, Y.; Fernandez, A.; Rojas, T.C.; Campora, J.; Palma, P.; Prozorov, R.; Gedanken, A. Encapsulation of Nickel Nanoparticles in Carbon Obtained by the Sonochemical Decomposition of Ni(C₃H₁₂)₂. *Chem. Mater.* **1999**, *11*, 1331–1335. [[CrossRef](#)]
15. Qiao, S.; Feng, C.; Guo, Y.; Chen, T.; Akram, N.; Zhang, Y.; Wang, W.; Yue, F.; Wang, J. CdS nanoparticles modified Ni@ NiO spheres as photocatalyst for oxygen production in water oxidation system and hydrogen production in water reduction system. *Chem. Eng. J.* **2020**, *395*, 125068. [[CrossRef](#)]
16. Mateo, D.; Albero, J.; Garcia, H. Graphene supported NiO/Ni nanoparticles as efficient photocatalyst for gas phase CO₂ reduction with hydrogen. *Appl. Catal. B Environ.* **2018**, *224*, 563–571. [[CrossRef](#)]
17. Ely, T.O.; Amiens, C.; Chaudret, B.; Snoeck, E.; Verelst, M.; Respaud, M.; Broto, J.-M. Synthesis of Nickel Nanoparticles. Influence of Aggregation Induced by Modification of Poly(vinylpyrrolidone) Chain Length on Their Magnetic Properties. *Chem. Mater.* **1999**, *11*, 526–529. [[CrossRef](#)]
18. Han, M.; Liu, Q.; He, J.; Song, Y.; Xu, Z.; Zhu, J.M. Controllable Synthesis and Magnetic Properties of Cubic and Hexagonal Phase Nickel Nanocrystals. *Adv. Mater.* **2007**, *19*, 1096–1100. [[CrossRef](#)]
19. Wang, H.; Jiao, X.; Chen, D. Monodispersed Nickel Nanoparticles with Tunable Phase and Size: Synthesis, Characterization, and Magnetic Properties. *J. Phys. Chem. C* **2008**, *112*, 18793–18797. [[CrossRef](#)]
20. Zach, M.P.; Penner, R.M. Nanocrystalline Nickel Nanoparticles. *Adv. Mater.* **2000**, *12*, 878–883. [[CrossRef](#)]
21. Winnischofer, H.; Rocha, T.C.R.; Nunes, W.C.; Socolovsky, L.M.; Knobel, M.; Zanchet, D. Chemical Synthesis and Structural Characterization of Highly Disordered Ni Colloidal Nanoparticles. *ACS Nano* **2008**, *2*, 1313–1319. [[CrossRef](#)] [[PubMed](#)]
22. Pan, Y.; Jia, R.; Zhao, J.; Liang, J.; Liu, Y.; Liu, C. Size-controlled synthesis of monodisperse nickel nanoparticles and investigation of their magnetic and catalytic properties. *Appl. Surf. Sci.* **2014**, *316*, 276–285. [[CrossRef](#)]
23. Carencio, S.; Boissiere, C.; Nicole, L.; Sanchez, C.; Le Floch, P.; Mézailles, N. Controlled design of size-tunable monodisperse nickel nanoparticles. *Chem. Mater.* **2010**, *22*, 1340–1349. [[CrossRef](#)]
24. Park, J.; Kang, E.; Son, S.U.; Park, H.M.; Lee, M.K.; Kim, J.; Kim, K.W.; Noh, H.J.; Park, J.H.; Bae, C.J.; et al. Monodisperse Nanoparticles of Ni and NiO: Synthesis, Characterization, Self-Assembled Superlattices, and Catalytic Applications in the Suzuki Coupling Reaction. *Adv. Mater.* **2005**, *17*, 429–434. [[CrossRef](#)]

25. Wang, S.; Zhang, L.; Li, X.; Li, C.; Zhang, R.; Zhang, Y.; Zhu, H. Sponge-like nickel phosphide–carbon nanotube hybrid electrodes for efficient hydrogen evolution over a wide pH range. *Nano Res.* **2017**, *10*, 415–425. [[CrossRef](#)]
26. Xu, J.; Schulte, A.; Schönherr, H.; Jiang, X.; Yang, N. Hierarchical Carbon Nanofibers@ Nickel Phosphide Nanoparticles for High-Performance Supercapacitors. *Small Struct.* **2022**, *3*, 2100183. [[CrossRef](#)]
27. Du, W.; Wei, S.; Zhou, K.; Guo, J.; Pang, H.; Qian, X. One-step synthesis and graphene-modification to achieve nickel phosphide nanoparticles with electrochemical properties suitable for supercapacitors. *Mater. Res. Bull.* **2015**, *61*, 333–339. [[CrossRef](#)]
28. Sawhill, S.J.; Layman, K.A.; Van Wyk, D.R.; Engelhard, M.H.; Wang, C.; Bussell, M.E. Thiophene hydrodesulfurization over nickel phosphide catalysts: Effect of the precursor composition and support. *J. Catal.* **2005**, *231*, 300–313. [[CrossRef](#)]
29. Gregg, K.A.; Perera, S.C.; Lawes, G.; Shinozaki, S.; Brock, S.L. Controlled Synthesis of MnP Nanorods: Effect of Shape Anisotropy on Magnetization. *Chem. Mater.* **2006**, *18*, 879–886. [[CrossRef](#)]
30. Park, J.; Koo, B.; Hwang, Y.; Bae, C.; An, K.; Park, J.-G.; Park, H.M.; Hyeon, T. Novel Synthesis of Magnetic Fe₂P Nanorods from Thermal Decomposition of Continuously Delivered Precursors using a Syringe Pump. *Angew. Chem. Int. Ed.* **2004**, *43*, 2282–2285. [[CrossRef](#)]
31. Park, J.; Koo, B.; Yoon, K.Y.; Hwang, Y.; Kang, M.; Park, J.-G.; Hyeon, T. Generalized Synthesis of Metal Phosphide Nanorods via Thermal Decomposition of Continuously Delivered Metal–Phosphine Complexes Using a Syringe Pump. *J. Am. Chem. Soc.* **2005**, *127*, 8433–8440. [[CrossRef](#)] [[PubMed](#)]
32. Henkes, A.E.; Schaak, R.E. Trioctylphosphine: A General Phosphorus Source for the Low-Temperature Conversion of Metals into Metal Phosphides. *Chem. Mater.* **2007**, *19*, 4234–4242. [[CrossRef](#)]
33. Mabayoje, O.; Dunning, S.G.; Kawashima, K.; Wygant, B.R.; Ciufo, R.A.; Humphrey, S.M.; Mullins, C.B. Hydrogen evolution by Ni₂P catalysts derived from phosphine MOFs. *ACS Appl. Energy Mater.* **2019**, *3*, 176–183. [[CrossRef](#)]
34. Xie, S.; Qiao, M.; Zhou, W.; Luo, G.; He, H.; Fan, K.; Zhao, T.; Yuan, W. Controlled Synthesis, Characterization, and Crystallization of Ni–P Nanospheres. *J. Phys. Chem. B* **2005**, *109*, 24361–24368. [[CrossRef](#)]
35. Carenco, S.; Resa, I.; Le Goff, X.; Le Floch, P.; Mézailles, N. White phosphorus as single source of “P” in the synthesis of nickel phosphide. *Chem. Commun.* **2008**, *14*, 2568–2570. [[CrossRef](#)] [[PubMed](#)]
36. Park, Y.; Kang, H.; Hong, Y.-K.; Cho, G.; Choi, M.; Cho, J.; Ha, D.-H. Influence of the phosphorus source on iron phosphide nanoparticle synthesis for hydrogen evolution reaction catalysis. *Int. J. Hydrogen Energy* **2020**, *45*, 32780–32788. [[CrossRef](#)]
37. Chiang, R.-K.; Chiang, R.-T. Formation of Hollow Ni₂P Nanoparticles Based on the Nanoscale Kirkendall Effect. *Inorg. Chem.* **2007**, *46*, 369–371. [[CrossRef](#)]
38. Henkes, A.E.; Vasquez, Y.; Schaak, R.E. Converting Metals into Phosphides: A General Strategy for the Synthesis of Metal Phosphide Nanocrystals. *J. Am. Chem. Soc.* **2007**, *129*, 1896–1897. [[CrossRef](#)]
39. Railsback, J.G.; Johnston-Peck, A.C.; Wang, J.; Tracy, J.B. Size-Dependent Nanoscale Kirkendall Effect During the Oxidation of Nickel Nanoparticles. *ACS Nano* **2010**, *4*, 1913–1920. [[CrossRef](#)]
40. Karmhag, R.; Niklasson, G.A.; Nygren, M. Oxidation kinetics of nickel nanoparticles. *J. Appl. Phys.* **2001**, *89*, 3012–3017. [[CrossRef](#)]
41. Lee, C.; Schmidt, L.D. Microstructures in Oxidation and Reduction of Small Ni Particles: Bubbles and Clusters. *J. Electrochem. Soc.* **1989**, *136*, 2471–2475. [[CrossRef](#)]
42. Yin, Y.; Rioux, R.M.; Erdonmez, C.K.; Hughes, S.; Somorjai, G.A.; Alivisatos, A.P. Formation of Hollow Nanocrystals Through the Nanoscale Kirkendall Effect. *Science* **2004**, *304*, 711–714. [[CrossRef](#)] [[PubMed](#)]
43. Cullity, B.; Stock, S. *Elements of X-ray Diffraction*, 3rd ed.; Prentice Hall: New York, NJ, USA, 2001; pp. 174–177.
44. Peng, S.; Sun, S. Synthesis and characterization of monodisperse hollow Fe₃O₄ nanoparticles. *Angew. Chem.* **2007**, *119*, 4233–4236. [[CrossRef](#)]
45. Son, S.U.; Jang, Y.; Park, J.; Na, H.B.; Park, H.M.; Yun, H.J.; Lee, J.; Hyeon, T. Designed synthesis of atom-economical Pd/Ni bimetallic nanoparticle-based catalysts for sonogashira coupling reactions. *J. Am. Chem. Soc.* **2004**, *126*, 5026–5027. [[CrossRef](#)] [[PubMed](#)]
46. Park, J.; Kang, E.; Bae, C.J.; Park, J.-G.; Noh, H.-J.; Kim, J.-Y.; Park, J.-H.; Park, H.M.; Hyeon, T. Synthesis, characterization, and magnetic properties of uniform-sized MnO nanospheres and nanorods. *J. Phys. Chem. B* **2004**, *108*, 13594–13598. [[CrossRef](#)]
47. Chen, D.-H.; Wu, S.-H. Synthesis of nickel nanoparticles in water-in-oil microemulsions. *Chem. Mater.* **2000**, *12*, 1354–1360. [[CrossRef](#)]
48. Knecht, M.R.; Garcia-Martinez, J.C.; Crooks, R.M. Synthesis, characterization, and magnetic properties of dendrimer-encapsulated nickel nanoparticles containing <150 atoms. *Chem. Mater.* **2006**, *18*, 5039–5044.
49. Sidhaye, D.S.; Bala, T.; Srinath, S.; Srikanth, H.; Poddar, P.; Sastry, M.; Prasad, B. Preparation of nearly monodisperse nickel nanoparticles by a facile solution based methodology and their ordered assemblies. *J. Phys. Chem. C* **2009**, *113*, 3426–3429. [[CrossRef](#)]
50. Roy, A.; Srinivas, V.; Ram, S.; De Toro, J.; Mizutani, U. Structure and magnetic properties of oxygen-stabilized tetragonal Ni nanoparticles prepared by borohydride reduction method. *Phys. Rev. B* **2005**, *71*, 184443. [[CrossRef](#)]
51. Reetz, M.T.; Maase, M. Redox-Controlled Size-Selective Fabrication of Nanostructured Transition Metal Colloids. *Adv. Mater.* **1999**, *11*, 773–777. [[CrossRef](#)]
52. Matsuda, J.; Yamamoto, T.; Takahashi, S.; Nakanishi, H.; Sasaki, K.; Matsumura, S. In Situ TEM Investigation of Structural Changes in Ni Nanoparticle Catalysts under Gas Atmospheres: Implications for Catalyst Degradation. *ACS Appl. Nano Mater.* **2021**, *4*, 2175–2182. [[CrossRef](#)]